Influence of coating parameters on oxidation behavior of Cr-coated zirconium alloy for accident tolerant fuel claddings

E.B. Kashkarov [a], D.V. Sidelev [a,*], N.S. Pushilina [a], J. Yang [b,c], C. Tang [b], M. Steinbrueck [b]

[a] National Research Tomsk Polytechnic University, School of Nuclear Science and Engineering, 634050 Tomsk, Russia
[b] Karlsruhe Institute of Technology, Institute for Applied Materials, Eggenstein-Leopoldshafen 76344, Germany
[c] Xi'an Jiaotong University, School of Energy and Power Engineering, 28 Xianning West Road, Xi'an 710049, China

ARTICLE INFO

Keywords:
Accident tolerant fuel
Chromium coating
Zirconium alloy
Magnetron sputtering
High-temperature oxidation
Microstructure

ABSTRACT

The Cr coatings (4.5–9.0 μm-thick) with porous/columnar and dense/columnar microstructure were deposited on Zr alloy. Oxidation was performed at 900, 1050, 1200 and 1400 °C in steam to define the role of coating microstructure and thickness on oxidation behavior of Cr-coated Zr alloy. The activation energy for chromium oxidation decreases from 249 to 124 kJ/mol when the coating microstructure changes from dense to porous. Both coatings types are consumed by Cr-Zr interdiffusion resulting in the similar thickness of residual Cr. The Cr-Zr interdiffusion can prevent forming the Cr oxide film and cause direct oxidation of the alloy at 1400 °C.

1. Introduction

In the last decades, there have been many studies to improve the oxidation resistance of Zr-based claddings for light water reactors (LWR) [1–4]. After the Fukushima-Daiichi accident occurred in 2011, several material strategies were suggested to develop effective and reliable cladding materials for accident tolerant fuel (ATF) under both normal operation (360 °C, 18.6 MPa) and accident (e.g. 1200 °C, water steam) scenarios. The short-term strategy of ATF development is the deposition of protective coatings on the outer surface of Zr-based claddings. Among a wide variety of coating materials, all promising concepts rely on the formation of a dense chromia, alumina and/or silica scale at high-temperature oxidation [5]. Therefore, any ATF coating should contain at least one of the elements such as chromium, aluminum or silicon. Nevertheless, coatings with high Al- or Si-content can become non-protective due to their hydrothermal dissolution in a water environment under normal operation conditions [6,7]. Oppositely, Brachet et al. [8] demonstrated the formation of a thin (~100 nm) Cr_2O_3 protective scale after 100 days of autoclave testing. Thereby, the Cr-based coatings can perform excellent oxidation performance under both normal operation and accident scenarios since the outer Cr_2O_3 layer acts as an efficient protective barrier. Moreover, the presence of chromium and/or chromia on the Zr cladding surface prevents not only oxygen but also hydrogen diffusion into the cladding as long as the coating remains intact [4,9].

Metallic Cr coatings attract much attention due to their high melting point, high oxidation resistance and thermal expansion coefficient similar to Zr alloys. A lot of studies demonstrated and approved the excellent oxidation performance of Cr-coated Zr alloys [3,4,8–20]. However, Cr coatings should not negatively impact the neutronic balance. Since chromium has higher (3.5 b) thermal neutron absorption coefficient than that of Zr alloys (0.2 b) [16], the thickness of Cr coatings should be limited to reduce the neutron flux losses. Moreover, it is important to enable high cracking resistance of the Cr coatings as any local cracks could be a short path for oxygen diffusion to the Zr alloy resulting in the enhanced oxidation of Zr claddings [8,21]. In this context, a large number of studies have been carried out to investigate the role of coating parameters and additional pre- or post-treatments on the oxidation resistance and mechanical behavior of Cr-coated Zr alloys. The comparative analysis of the Cr-coated Zircaloy-4 (Zry-4) alloy after steam oxidation at 1100 °C [8] revealed the reduction of the mass gain from 7 to < 1 mg/cm^2 with increasing the thickness of the Cr coatings from 1 to 10 μm. The microstructure of the Cr coatings can be the key parameter in accidental conditions as long as the coating remains protective [11,15]. The increase in grain size of Cr coatings by additional annealing at 700 and 800 °C improves their oxidation resistance in steam [12]. Nevertheless, the pre-annealing temperature of the coated Zr alloys should be less than the annealing temperature of the commercially used Zr alloy cladding tubes, which is at about 500 °C [22]. The effect of preliminary oxidation of Cr-coated Zr claddings in

* Corresponding author.
E-mail address: sidelevdv@tpu.ru (D.V. Sidelev).

supercritical water (345 °C and 16.5 MPa) on their oxidation behavior was examined in [13]. He et al. found the nonmonotonic relationship between the gas pressure, the bias potential and the oxidation performance [14]. The high oxidation resistance of Cr coatings with (110) texture was shown in [17]. Oxidation and degradation of the Cr-coated Zircaloy in steam up to 1600 °C were investigated in transient experiments with plate samples [20] as well as under more prototypical conditions with cladding tube segments [23]. Cracking behavior and fracture properties of Cr-coated Zr alloys were examined by both scanning electron microscopy [18] and in-situ three-point bending test [19]. So, the published results have described a lot of aspects of Cr coating deposition influencing their oxidation behavior and microstructural evolution. However, the deposited Cr coatings mainly have a columnar structure that is undesirable since it significantly decreases corrosion resistance of the coatings due to the rapid diffusion of oxygen along the grain boundaries into the Zr alloy. There are no systematical data showing a clear comparison between Cr coatings with the same thickness and different microstructure in a wide range of temperatures. Moreover, it is not fully understood how coating microstructure can affect the interdiffusion of Cr and Zr depending on their microstructure type. Thus, a more comprehensive analysis of the role of both coating thickness and microstructure on their oxidation behavior is still required.

In the current study, six series of Cr coatings with porous/dense columnar microstructure and thicknesses of ~4.5, 6.0 and 9.0 μm were deposited on the zirconium alloy by magnetron sputtering. The isothermal oxidation tests in a steam environment were performed at 900, 1050, 1200 and 1400 °C. The cross-section microstructure and weight gain of the samples are compared after the oxidation tests for the different coating series. Then, oxidation behavior and microstructural changes of the Cr coatings deposited on Zr alloy are discussed.

2. Materials and methods

2.1. Sample preparation

Chromium coatings were deposited on E110 (Zr-1%Nb) alloy sheets ($15 \times 15 \times 2$ mm^3) and polished Si (110) substrates using magnetron sputtering. Two types of magnetron sputtering systems were used in experiments to obtain different microstructures of the Cr coatings. The first type is a multi-cathode sputtering system with cooled Cr targets, and the second is a hot Cr target sputtering system. Cr targets (⌀ 90×8 mm^2, JSC "Polema", Russia) with a purity of 99.95% were used. The detailed description of the deposition equipment and ion-plasma installation has been reported in a previous study [9]. The description about the hot Cr target sputtering system for Cr coating deposition is in ref. [24]. The samples were polished using SiC sandpapers (P1200→P2500, Hermes, UK), rinsed with acetone and dried by compressed air. To hold the samples during the oxidation tests, holes with diameter of ⌀1 mm were drilled near the corner of samples.

The residual pressure in the vacuum chamber was 5×10^{-3} Pa. Before deposition, the samples were treated by Ar^+ ions for 20 min at the following parameters: Ar pressure – 0.15 Pa, voltage – 2.5 kV, ion current – 40 mA. All samples were planetary-rotated during ion treatment and coating deposition. The deposition conditions of the Cr coatings are shown in Table 1. Six series of the Cr-coated E110 alloy sheets were prepared. Coating deposition was performed in Ar (99.999%) atmosphere at a pressure of 0.3 Pa. No preliminary or additional heating of the samples was carried out, and their temperature was measured by an infrared pyrometer Optris CTlaser 3MH1CF4. The samples were fixed in stainless steel holders during coating deposition, thus, a small area of the Zr sheets (~8–9 mm^2) remained uncoated.

2.2. Steam oxidation tests

Four types of the oxidation tests (Run no. 1–4) were performed in this study (Table 2). The uncoated Zry-4 sheets ($15 \times 10 \times 0.65$ mm^3) were also oxidized as the reference material for comparative analysis.

The Runs #1–3 were done using a thermogravimetric analyzer (TGA) STA 449 F3 (NETZSCH) with a steam generator coupled to a mass spectrometer (NETZSCH Aeolos). This system provides in-situ measurements of the mass gain of the samples and concentration of the emission gases during the oxidation tests. The heating and cooling of the samples until the isothermal oxidation stage were done in a protective Ar environment with a flow rate of 50 mL/min. The temperature of the isothermal oxidation was stabilized during 1 min before injecting the 100% steam flow (2 g/h). The isothermal oxidation tests were performed at 900, 1050 and 1200 °C for 30, 20 and 10 min, respectively.

The Run #4 is a steam oxidation test at 1400 °C, which was done using a horizontal tube furnace [25]. The samples were heated in protective Ar atmosphere up to 1400 °C, then the temperature was stabilized during 1 min. After it, the steam was injected in the tube furnace. The Ar flow rate in this furnace was 20 L/h, the steam flow rate of 20 g/h resulting in a steam concentration of 35.9 wt% (55.4 mol.%). The mass-spectrometer was connected to the tube furnace to record the hydrogen output during the oxidation reaction between steam and samples. The mass gain of the samples was determined by measuring their mass before and after the test using an analytical balance (AE 240, Mettler). The concentration of hydrogen formed during the oxidation tests was used to determine in-situ mass gain of the samples according to the procedure described in [26]. It should be noted that hydrogen absorption can have a minor effect on the overall kinetics during HT oxidation process.

Table 1
The deposition conditions of the Cr coatings.

Sample	Target power density, W/cm^2	Deposition time, min	Magnetron type	Coating thickness, μm	Sample temperature, °C
Cr-4.5d	31.4	128	multi-cathode	4.5 ± 0.1	330
Cr-6d		170		6.0 ± 0.2	335
Cr-9d		256		9.0 ± 0.3	345
Cr-4.5c	39.5	15	with hot Cr target	4.5 ± 0.3	320
Cr-6c		20		6.0 ± 0.2	380
Cr-9c		30		9.0 ± 0.2	440

Note: "d" represents dense columnar microstructure; "c" represents porous columnar microstructure.

2.3. Sample characterization

The thickness of the as-deposited Cr coatings, cross-section microstructure and elemental composition of the samples after oxidation tests were examined using a scanning electron microscope (SEM) Vega 3 (Tescan, Czech Republic) equipped with energy-dispersive X-ray spectroscopy (EDX) attachment. The microstructure of the oxidized samples was additionally analyzed by an optical microscopy using AXIOVERT-200 MAT (Zeiss, Gottingen, Germany). The depth distribution of elements was studied by glow discharge optical emission spectroscopy using a GD-Profiler 2 (HORIBA Scientific, Japan).

Table 2
Parameters of steam oxidation tests.

Run	Temperature, °C	Exposure time, min	Heating facility	Heating/cooling rate in Ar, °C/min
1	900	30	TGA	20/100
2	1050	20	TGA	20/100
3	1200	10	TGA	20/100
4	1400	5	Tube furnace	10/10

3. Results and discussion

3.1. Cross-section microstructure of the as-deposited Cr coatings

Fig. 1 shows the cross-section microstructures of the as-deposited Cr coatings obtained on Si substrates. Six series of the Cr coatings with a thickness of 4.5 (Fig. 1a, b), 6.0 (Fig. 1c, d) and 9.0 μm (Fig. 1e, f) were prepared.

It was found that the Cr coatings had a different microstructure depending on the type of the magnetron sputtering system. A porous columnar microstructure of the Cr coatings is clearly observed for the samples obtained by hot target magnetron sputtering (Fig. 1a, 1c and e). This type of the Cr coatings has pronounced V-shape columns through a coating thickness. Such coating microstructure can be attributed to zone T according to the structure zone model [27]. The deposition of porous Cr coatings is due to low energy flux per one deposited atom for hot target sputtering [10,11]. Oppositely, the Cr coatings deposited by multi-cathode magnetron sputtering system with cooled Cr targets are characterized by a dense columnar microstructure (Fig. 1b, d and f). The growth of dense Cr coatings can be attributed to high values of energy flux per one deposited atom for multi-cathode sputtering and "knock-on" effect [28]. The role of magnetron type on the cross-section microstructure of the Cr coatings was analyzed and discussed in detail in our previous study [11]. In this article for simpler comparison of the porous/columnar and dense/columnar Cr coatings, they will be hereinafter referred to as “columnar” and “dense”.

3.2. High-temperature oxidation in steam at 900–1200 °C

Fig. 2 shows the mass gain of the Cr-coated Zr alloy during and after steam oxidation at 900, 1050 and 1200 °C.

Parabolic kinetics is observed for Cr-coated Zr alloy samples during the stage of continuous oxidation at 900 and 1050 °C with some deviations at the end of the oxidation for 4.5 and 6 μm-thick Cr coatings (Fig. 2a and b). The mass gain curves have a transition from protective to non-protective scale, which is clearly visible at 1200 °C (Fig. 2c) [11, 12]. This is caused by an acceleration of oxidation kinetics and can be determined as the time of transition period signed in Fig. 2c for 4.5 and 6.0 μm-thick Cr coatings. Generally, the rate constants (K_p) of the samples with the dense Cr coatings are less than that of the samples with columnar coatings. Two exceptions of this trend belong to 9 μm-thick Cr coatings in the case of oxidation at 900 and 1050 °C. Most likely that it is

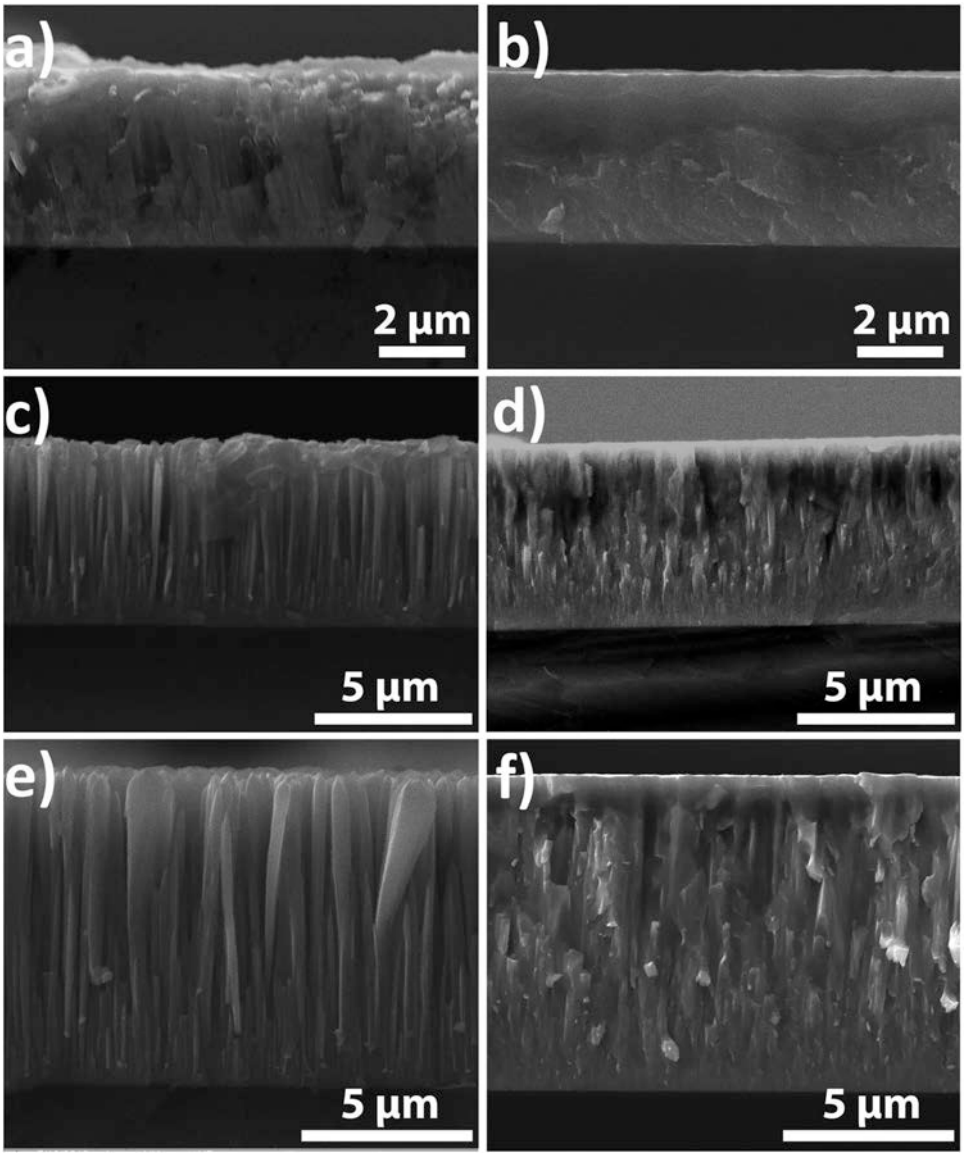

Fig. 1. Cross-section microstructures of the as-deposited Cr coatings: Cr-4.5c (a); Cr-4.5d (b); Cr-6c (c); Cr-6d (d); Cr-9c (e) and Cr-9d (f).

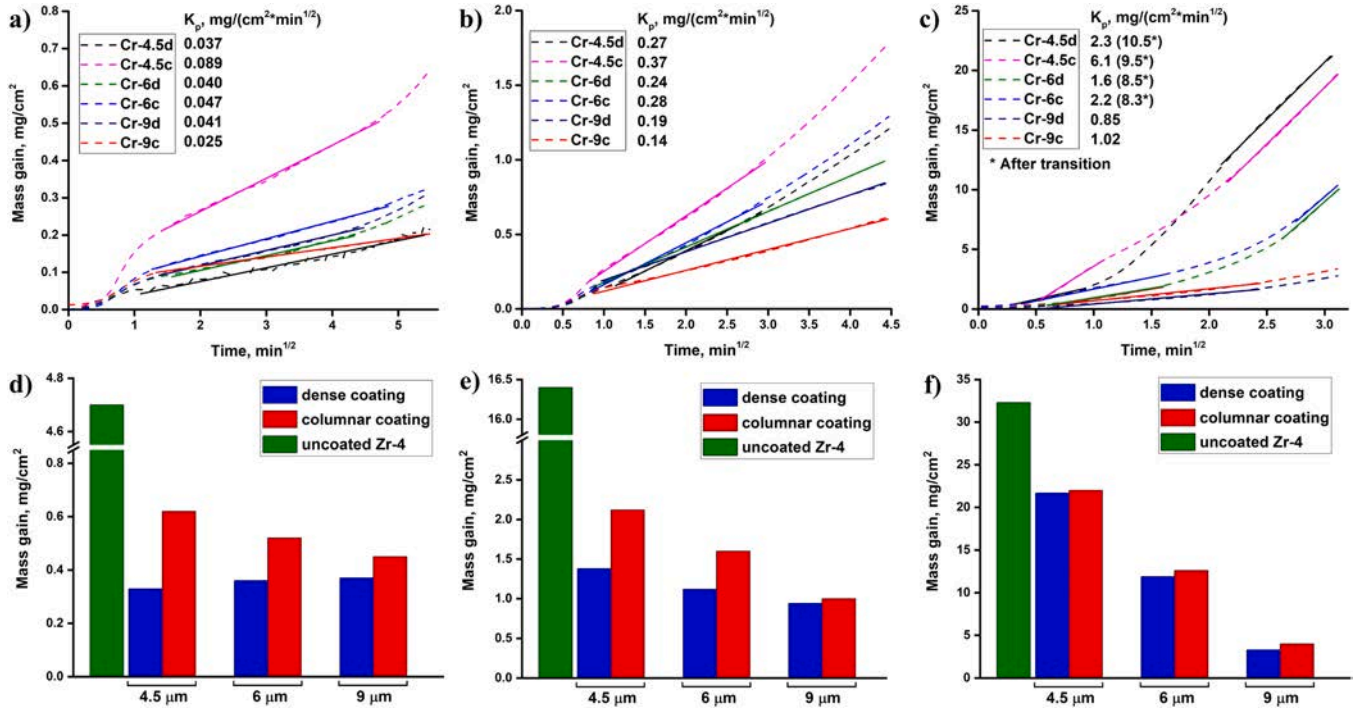

Fig. 2. Mass gain evolution of the samples during isothermal oxidation and measured using the analytical balance after the oxidation tests at 900 (a, d), 1050 (b, e) and 1200 °C (c, f). *- Rate constant after transition from protective to non-protective scale.

caused by forming thinner Cr_2O_3 layer on the samples with dense Cr coating during the heating stage of the oxidation test due to a presence of residual oxygen in the chamber. Then, faster oxidation of the dense Cr coatings can be during the isothermal oxidation stage.

The protective properties of the Cr coatings are clearly seen since the higher mass gain of the uncoated Zr alloy was found in comparison with the Cr-coated ones. According to Fig. 2, the samples with dense Cr coatings have lower mass gains than that of Zr alloy coated by columnar coatings in the considered range of temperatures (900–1200 °C). However, as the oxidation temperature was increased, the difference of mass gains between columnar and dense Cr coatings became less. For example, the difference of the mass gains between 4.5 μm-thick Cr coatings decreased from 97% to 2% for 900→1200 °C, respectively. On the contrary, the effect of coating thickness appeared at the high temperature (1200 °C). After the oxidation test at 900 °C, the mass gain of the samples had the minor range of the values: for the dense Cr coatings - 0.33–0.37 mg/cm^2 and for columnar ones - 0.45–0.65 mg/cm^2. However, when the oxidation temperature increased, the effect of coating thickness became more pronounced. The mass gains of the samples with the dense coatings were equal to 3.3, 11.9 and 21.7 mg/cm^2 for 4.5, 6.0 and 9.0 μm-thick Cr coatings after the oxidation test at 1200 °C, in the case of the columnar coatings - 4.0, 12.6 and 22 mg/cm^2, respectively. Therefore, among the experimental samples, the Cr-9d sample demonstrated the best oxidation resistance as this sample had the lowest mass gain after steam oxidation at 900–1200 °C. The Cr-4c sample with the lowest coating thickness and columnar microstructure showed the largest mass gain in all TGA tests.

Fig. 3 shows the cross-section SEM microstructure and corresponding EDS-lines of 9 μm-thick Cr coatings on Zr alloy after oxidation at 1200 °C for 10 min Table 3 presents the content of Cr, Zr and O in cross-

Table 3
The content of Cr, Zr and O in Zr alloy with 9 μm-thick Cr coatings after steam oxidation test at 1200 °C for 10 min.

Points	1	2	3	4	5	6	7	8	9	10
Cr, at%	97	75	28	14	16	94	78	2	1	18
Zr, at%	2	24	70	86	83	1	19	89	89	81
O, at%	1	1	2	0	1	5	3	9	10	1

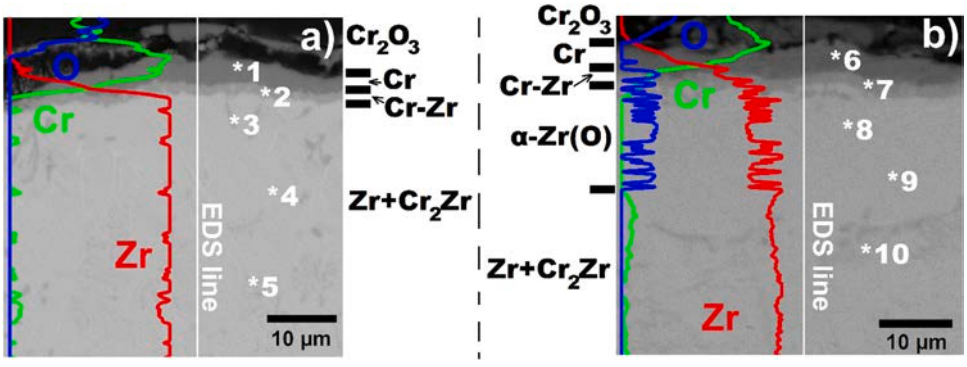

Fig. 3. SEM images and corresponding EDS-lines of 9 μm-thick Cr coatings with the dense (a) and columnar (b) microstructure on Zr alloy after oxidation at 1200 °C for 10 min.

section microstructure of these samples.

It is well seen that both samples have the typical layered structure that is composed of the outer Cr_2O_3, residual Cr and Cr-Zr interdiffusion layers. The thicknesses of these layers are dependent on the coating type. Moreover, the dense and columnar Cr coatings have a different depth distributions of Cr, Zr and O underneath the Cr-Zr interdiffusion layer. No oxygen signal is found in this region for the sample with the dense Cr coating, while the weak peaks of Cr are observed in the Zr alloy starting from the Cr-Zr interface and continued into the depth of Zr alloy. In contrast, the sample with the columnar Cr coating exhibits a continuous signal of O within ~20 μm underneath the Cr-Zr interface attributed to the formation of α-Zr(O). Below the weak signal of Cr appears and continues into the depth of Zr alloy. To define the role of coating type on chromium oxidation and Cr-Zr interdiffusion, the cross-section microstructure of all Cr-coated Zr alloy samples after oxidation tests was examined by SEM. For calculations of the oxidized Cr layer (h_{oxide}), the Pilling-Bedworth index was used (~2 for $Cr \rightarrow Cr_2O_3$ transition [12,29]). The thickness of residual Cr layer (h_{res}) was determined by SEM after the oxidation tests. The Cr layer consumed by the Cr-Zr interdiffusion was calculated by the following equation:

$$h_{dif} \quad h_{in} - h_{oxide} - h_{res}, \tag{1}$$

where h_{in} – the initial thickness of the as-deposited Cr coatings. The consumption of Cr by the Cr-Zr interdiffusion results in the formation of intermetallic phase $ZrCr_2$ at the interface and the Cr diffusion into the bulk alloy leading to $ZrCr_2$ precipitates (during cooling). The diagrams of Cr coating consumption on oxidation and Cr-Zr interdiffusion (in %) depending on their initial thickness (4.5, 6.0 and 9.0 μm) and oxidation conditions are shown in Fig. 4.

It is evident that the thickness of the Cr oxide layer increased when the oxidation temperature changed from 900 to 1200 °C. The samples with columnar Cr coatings had higher thickness of Cr layer consumed by oxidation than that of the samples with the dense Cr coatings. This is caused by accelerated oxygen diffusion along the columns of the Cr coatings [30]. As expected, the thickness of the residual Cr layer is higher for thicker coatings. The Cr-Zr interdiffusion also affects the thickness of the residual Cr layer. Higher diffusion of Cr and Zr at higher temperature results in thicker Cr-Zr interdiffusion layer at the interface and more Cr atoms diffused into the bulk alloy. The significant role of temperature on Cr-Zr interdiffusion kinetics for the relatively short time was described in [31]. In this paper, the experimental data show that the dense Cr coatings had the higher proportion of Cr transformed to Cr-Zr layer in comparison with the columnar ones. The phase composition of Zr alloy underneath the Cr coatings can strongly influence Cr-Zr interdiffusion kinetics as solubility and diffusion rate of Cr in β-Zr is higher than that of α-Zr [32]. Due to this, the samples with the columnar Cr coatings had less thickness of Cr-Zr layer as oxygen penetrates to the alloy and can stabilize the α-Zr phase that slows down Cr-Zr interdiffusion. The deceleration of Cr-Zr interdiffusion was also found in high-temperature oxidation tests (1330–1400 °C) of the CrN/Cr-coated E110 alloy when the α-Zr(N) phase was grown underneath the coatings due to CrN decomposition [33]. Moreover, the different kinetics of Cr-Zr interdiffusion was also observed for the Cr coatings obtained by cold spraying in comparison with the magnetron-deposited ones [31]. In the above paper, the difference in Cr-Zr interdiffusion kinetics was explained by the presence of thin oxide layer (ZrO_x) at the coating-alloy interface, which can be formed during coating deposition. The effect of Cr coating microstructure on Cr-Zr interdiffusion is well seen from the comparative SEM images and EDS maps of the 9 μm-thick Cr coatings with the dense and columnar microstructure after steam oxidation at 1050 °C for 20 min (Fig. 5). The overlapping of the O (K-α) and Cr (L-α) EDS peaks resulting in overestimated oxygen signals in Cr and O area maps should be taken into account for the analysis. The lower thickness of the Cr-Zr interlayer was determined in the case of the columnar Cr coating in comparison with the dense one.

According to Fig. 4, the thicknesses of the residual Cr layers after oxidation tests are equal to 8.0 ± 0.5 and 7.3 ± 0.4 (after 900 °C), 7.0 ± 0.3 and 6.6 ± 0.6 (after 1050 °C), 4.4 ± 0.6 and 4.0 ± 0.4 μm (after 1200 °C) for the dense and columnar Cr coatings, respectively. Interestingly, the thicknesses of the remaining Cr layers after oxidation tests at the respective temperature (900, 1050 or 1200 °C) are the similar for both coating types. The difference in the thicknesses of the residual Cr layers is less than 9%. The consumption of the columnar Cr is larger by oxidation of the outer surface of the Cr coatings, while the dense Cr coatings are significantly consumed on Cr-Zr interdiffusion. Moreover, at long oxidation times, Cr solubility in β-Zr alloy can have a high impact on the duration of the protective state of Cr-coated Zr alloys [31]. It will shorten the protective period even in the case of the dense Cr coating, as the thickness of the residual Cr layer will decrease due to the Cr-Zr interdiffusion. Therefore, some attention should be paid to developing special approaches to stabilize the α-Zr phase under Cr coatings of at least a small thickness. This approach can help to slow down the kinetics of Cr-Zr interdiffusion and increase the duration of the protective state for Cr-coated Zr alloys. However, oxygen inward diffusion will brittle

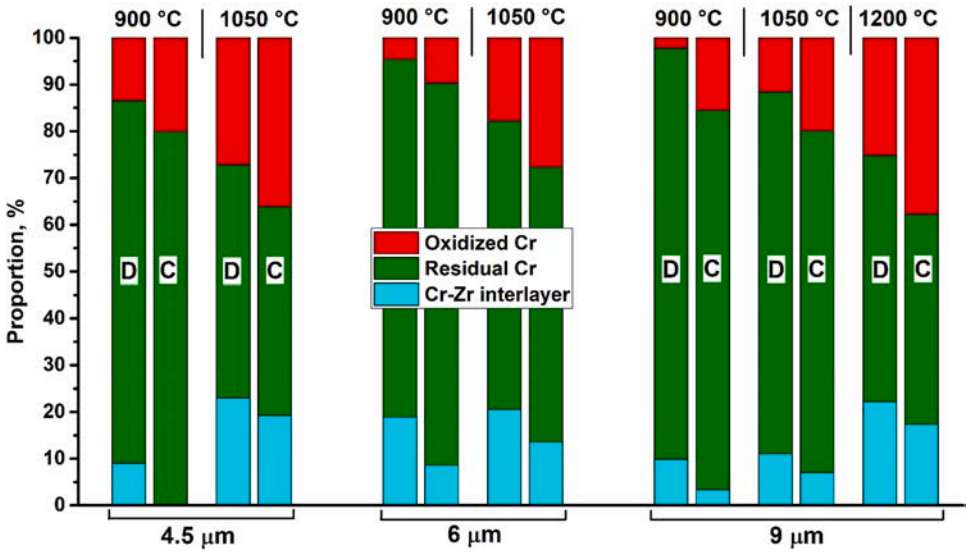

Fig. 4. Proportions of coating consumption on oxidation and interdiffusion for the dense (D) and columnar (C) Cr coatings depending on initial coating thickness and oxidation temperature.

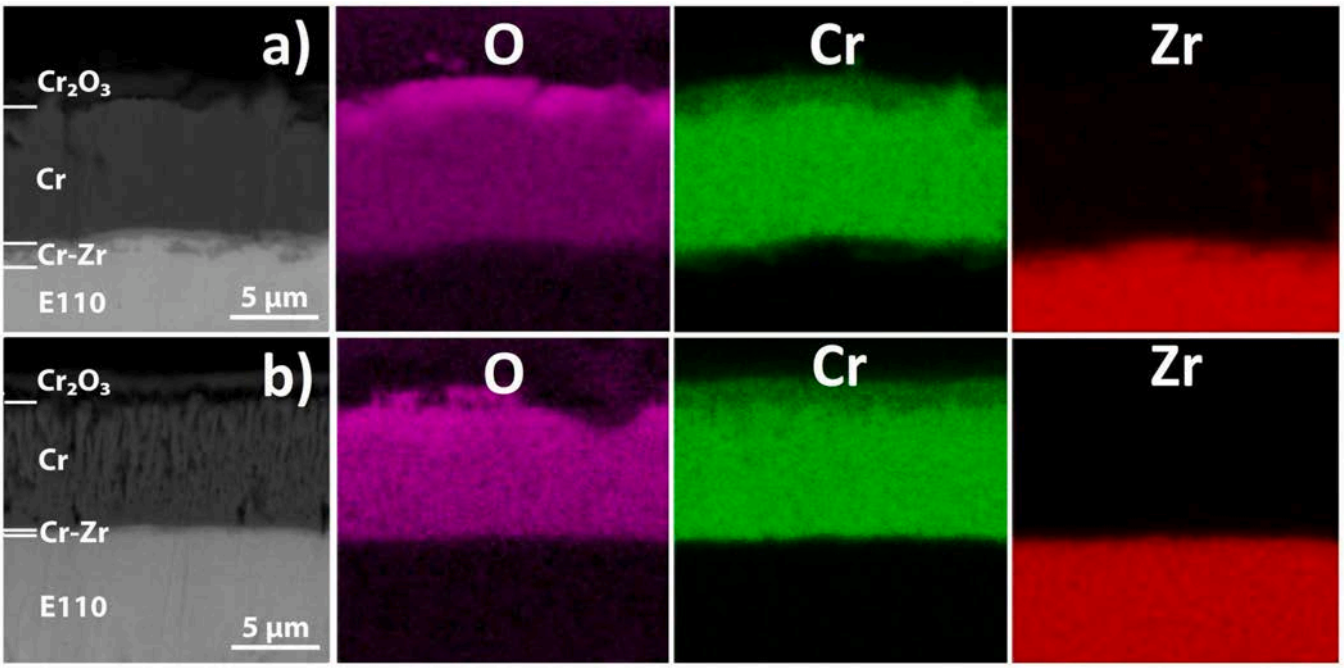

Fig. 5. SEM images and corresponding EDS maps of 9 μm-thick Cr coatings with the dense (a) and columnar (b) microstructure after oxidation at 1050 °C for 20 min.

the Zr alloy decreasing the residual structural integrity of the Zr claddings [34].

To determine the oxidation kinetics of the Cr coatings depending on their microstructure, the two series of the 9 μm-thick Cr coating were considered as they were protective under the current oxidation conditions. It is known [35] that the growth of Cr_2O_3 scale can be described by a parabolic law:

$$h(Cr_2O_3) \quad [K_p \bullet t]^{1/2}, \tag{2}$$

where $h(Cr_2O_3)$ – the thickness of the chromia (m); K_p – the rate constant (m^2/s); t – the oxidation time (s). The linear curves of ln(Kp) vs. ($1/T$) for the Cr coatings are fitted according to the Arrhenius equation:

$$K_p \quad A \bullet \exp\left(\frac{E_a}{R \bullet T}\right), \tag{3}$$

where A – the pre-exponential constant (m^2/s); E_a – the activation energy for oxidation process (J/mol); R – the gas constant (8.31 J/mol K); T – the temperature (K). The calculated rate constants for the experimental samples are shown in Fig. 6.

The obtained K_p values calculated for the experimental samples are in good agreement with the published data for oxidation of Cr-coated zirconium alloy in a steam environment [12]. It can be observed that the behavior of K_p values for the Cr coatings demonstrates the role of coating microstructure on chromium oxidation kinetics. The calculated activation energy is 124 and 249 kJ/mol, the pre-exponential constant is equal to $1.2{\cdot}10^{-9}$ and $2.7{\cdot}10^{-5}$ m^2/s for the columnar and dense Cr coatings, respectively. Such a large difference in E_a results in better oxidation resistance of dense Cr coatings.

3.3. High-temperature oxidation in steam at 1400 °C

Fig. 7a shows the hydrogen output curves during steam oxidation of Cr-coated E110 alloy samples at 1400 °C for 5 min. These data were converted into mass gain of the samples (Fig. 7b). The uncoated Zr-4 alloy was also oxidized in a steam environment as the reference material.

According to Fig. 7, all Cr coatings did not affect the oxidation kinetics of the Cr-coated Zr alloy at 1400 °C. A sharp increase of the

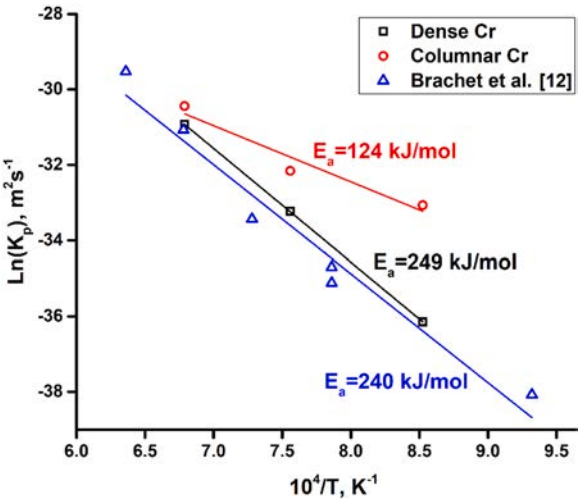

Fig. 6. Arrhenius plots of the rate constant of the parabolic law describing the growth of Cr_2O_3 scale in a steam environment for the columnar and dense Cr coatings in the present study and derived from [12].

hydrogen generation is observed up to ~0.03 mg/(s•cm^2) when the steam was injected into the tube furnace. Then the H_2 generation decreased gradually to 0.005 mg/(s•cm^2) during the isothermal oxidation. The uncoated and Cr-coated Zr alloy samples had similar kinetics of mass gain changing under isothermal oxidation. The mass gain of the samples after the oxidation test at 1400 °C measured by analytical balance is shown in Table 4. These data correlate well with the calculated ones shown in Fig. 7b.

The appearance of the samples after their oxidation at 1400 °C for 5 min is shown in Fig. 8.

Blisters are found on the outer surface of the Cr-6d and Cr-9d samples. For the Cr-6d sample, only one huge blister was located on the right top corner, while the multiple blisters on the Cr-9d continuously distributed over the sample surface. The formation of the "crocodile skin"-like morphology is caused by the Zr-Cr eutectic reaction that

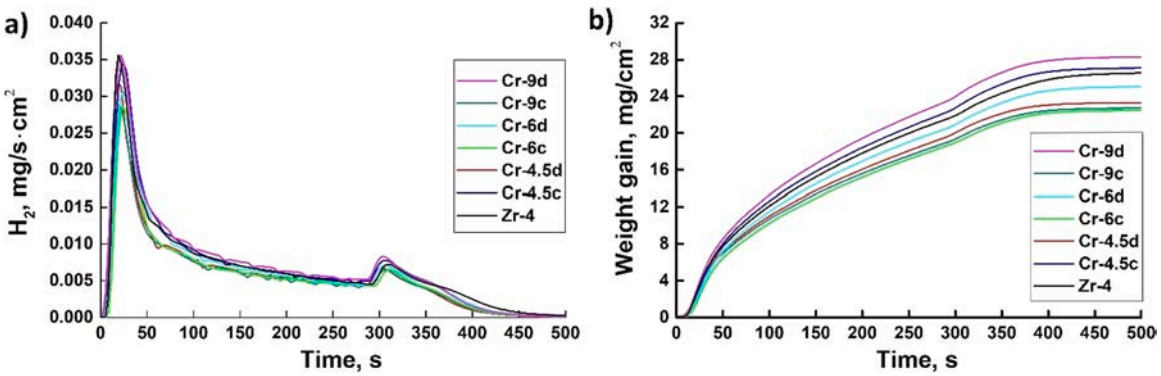

Fig. 7. The hydrogen output (a) and in-situ mass gain (b) of the samples vs. oxidation time.

Table 4
Mass gain of the samples after steam oxidation test at 1400 °C for 5 min.

Sample	Cr-4.5d	Cr-6d	Cr-9d	Cr-4.5c	Cr-6c	Cr-9c	Zr-4
Mass gain (mg/cm^2)	27.3	25.0	27.5	27.6	26.1	26.6	28.4

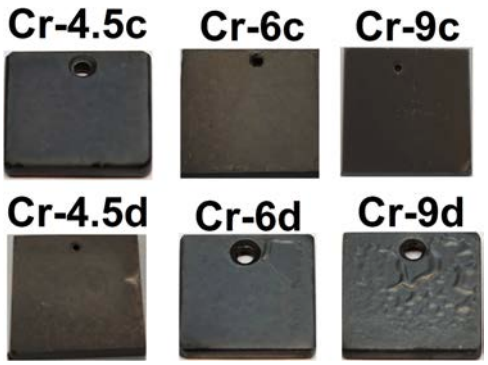

Fig. 8. The appearance of the samples after steam oxidation test at 1400 °C for 5 min.

occurs at temperatures around 1332 °C [36]. No blisters were found on the Cr-4.5d sample and E110 alloy samples with the columnar Cr coatings. To get more insights into morphology changes of the Cr-coated E110 alloy samples, three samples were selected for more detailed examinations. Fig. 9 demonstrates SEM images and corresponding EDS maps of the Cr-9d sample after the steam oxidation at 1400 °C.

Based on the SEM and EDS results, several layers can be distinguished in the cross-section microstructure of the Cr-coated Zr alloy. The outer ZrO_2 layer was non-uniform and its thickness varied from 70 to 120 μm. Underneath, a 250 μm-thick α-Zr(O) layer with smooth interfaces was formed. The layer below consists of chromium-depleted prior β-Zr dendrites and chromium-enriched inter-dendritic zones that was also found for high-temperature steam oxidation beyond 1300 °C [12] and in the transient tests (up to 1600 °C) [20]. The inner part of the alloy is the prior β-Zr phase. Moreover, cracks are observed inside the oxide layer. Most likely that the cracking was caused by high internal stresses in the surface region generated by oxidation of the Zr alloy as well as due to the difference between the lattice parameters of newly formed phases (ZrO_2 and $ZrCr_2$). Despite the absence of the blisters on the surface of the Cr-4.5d and Cr-9c samples, the same layered structure is observed in Fig. 10 as it was shown in Fig. 9. Both samples have the similar thickness of ZrO_2 (70 μm) and oxygen-stabilized α-Zr (205 μm) layers, and the $ZrCr_2$ +Zr zone with the dendrite-like structure is also placed underneath.

All samples did not have outer Cr_2O_3 layer which is usually observed for Cr-coated Zr alloys after high-temperature oxidation in water vapor

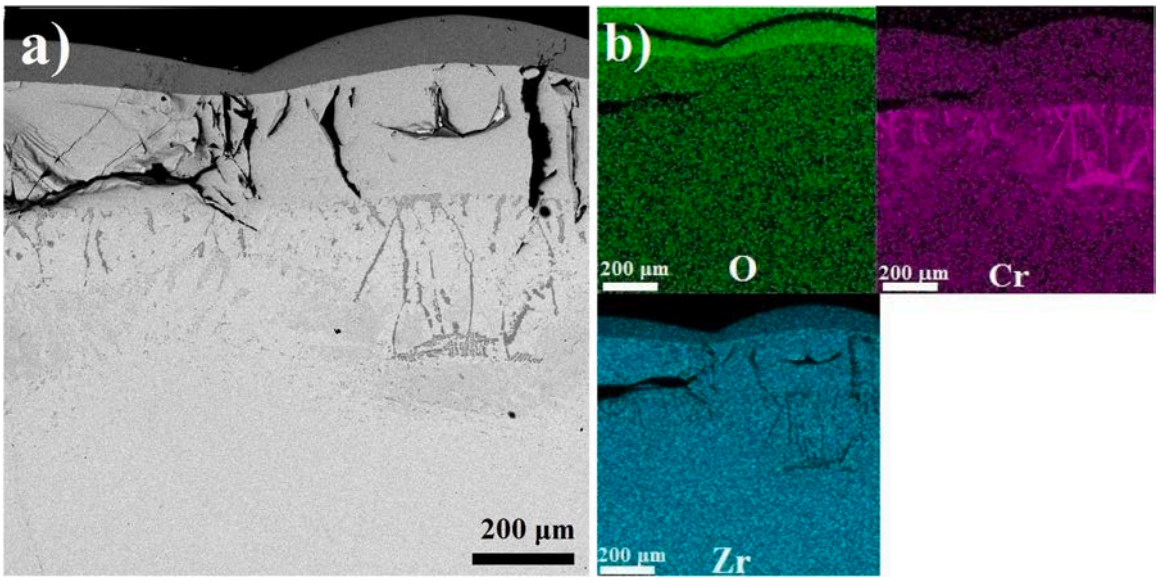

Fig. 9. Cross-section microstructure (a) and corresponding EDS maps (b) of the Cr-9d sample after steam oxidation at 1400 °C for 5 min.

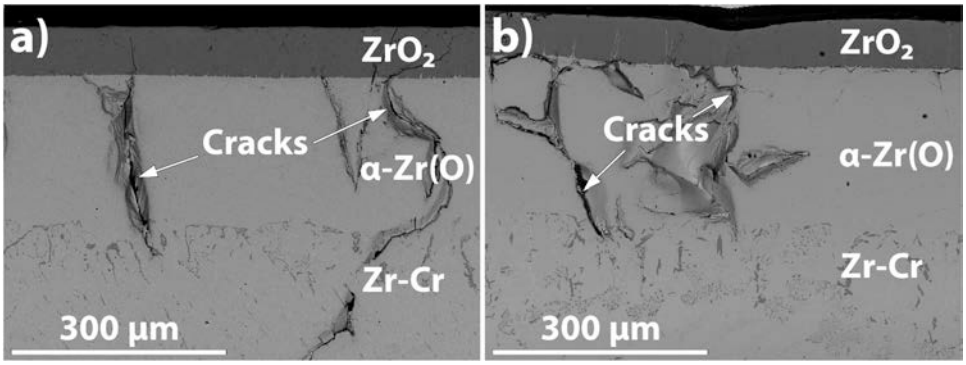

Fig. 10. Cross-section SEM images of the Cr-4.5d (a) and Cr-9c (b) samples after the steam oxidation at 1400 °C for 5 min.

[8,11,12]. In previous studies [37,38], X. Han et al. showed the reduction stage for oxidation of Cr-coated Zry-4, when the redox process of Cr_2O_3 layer by Zr alloy can occur. This mechanism leads to forming ZrO_2 layer underneath Cr coating. The growth of mixed oxide (Cr_2O_3 and ZrO_2) zone due to the reduction reaction was found in high-temperature transient experiments [20]. XRD study and EDS surface analysis of the Cr-9d sample indicate no presence of Cr in a surface region after steam oxidation at 1400 °C (Fig. 11). So, most likely that the formation of layered structure (observed in Fig. 10) is caused by full consuming of Cr coating by Zr alloy due to rapid Cr-Zr interdiffusion until the isothermal oxidation stage was started.

Due to the low heating rate (10 °C/min) of the samples in Ar atmosphere, rapid interdiffusion of Cr-Zr occurred until the isothermal oxidation stage was started. Two stages of Cr-Zr interdiffusion can be highlighted in the range from room temperature to 1400 °C. The first stage is upon heating up to 1330 °C, when the initial Cr layer can be consumed by diffusion and dissolution in the β-Zr alloy. The thickness of the residual Cr layer can be calculated by the modified parabolic law suggested by Yang et al. [31]. Using the rate constants for the Cr coatings from [31], the thickness of the residual Cr layer can be estimated as ~2.1, 3.6 and 6.6 μm for the coatings with initial thicknesses of 4.5, 6.0 and 9.0 μm, respectively. The second stage is started at the Cr-Zr eutectic temperature (1330 °C), when the Zr-Cr liquid phase is formed by the reaction between $ZrCr_2$ and β-Zr phases. For this stage, the increase in diffusion rates of Cr and Zr will be caused by higher temperature as well as due to forming the liquid Cr-Zr phase. To confirm this, one additional test was performed which consisted of annealing of the Zr alloy with the dense 9 μm-thick Cr coating in pure Ar at 1400 °C with heating/cooling rates of 10 °C/min. The cross-section SEM microstructure and depth distribution of Cr, Zr and Nb obtained by a glow discharge optical emission spectroscopy are shown in Fig. 12.

According to Fig. 12, the Cr coating was fully consumed by Cr-Zr interdiffusion as the signal of Cr is firstly observed only in the Zr alloy at a depth of ~18 μm and then continues into the depth of the Zr alloy. The EDS analysis of the cross-section microstructure showed that Cr is mainly concentrated in small regions represented by the chromium-enriched precipitates (Table 5) as it was discussed earlier.

Therefore, taking into account the above-mentioned result (Fig. 12) and the same thicknesses of ZrO_2, α-Zr(O), and Cr-Zr layers in the samples with the 4.5 and 9.0 μm-thick Cr coatings after steam oxidation at 1400 °C (Figs. 9 and 10), the samples should have a similar state, when the final oxidation temperature of 1400 °C was reached. Due to different initial thicknesses of the Cr coatings, this could occur only if the Cr coatings had been fully consumed by Cr-Zr interdiffusion to form the liquid phase and being diffused in the Zr alloy, when the isothermal oxidation was started. This resulted in no protective Cr oxide film under oxidation, and oxygen could directly react with the Zr alloy to form the ZrO_2 and α-Zr(O) layers. Such mechanism is confirmed by the equal behavior of hydrogen output curves for uncoated and Cr-coated samples during the isothermal tests at 1400 °C (Fig. 7). The injecting of water vapor in the tube furnace at 1400 °C leaded to the fast oxidation of Zr alloy as chromium had diffused in the alloy. It caused the sharp increase of H_2 generation in the start period of the oxidation test and next decrease of H_2 output as newly-formed outer ZrO_2 layer can limit alloy oxidation.

In view of higher solubility and diffusion rate of Cr in β-Zr than that of α-Zr [32], Cr would diffuse deeper in the Zr alloy when oxide layers in the Zr alloy are grown. When the samples began to cool down, the Zr-Cr liquid phase solidified and some blisters formed leading to the "crocodile skin" like morphology on the surface of the samples due to the volume changes associated with solid → liquid → solid reactions.

The presence of blisters only in the samples with the dense Cr coatings can be caused by higher chromium concentration and different diffusion rate in the alloy compared with the columnar ones as the latter had less density and another coating microstructure in the as-deposited state (Fig. 1). This statement is also confirmed by the fact that the Cr-9d coating (9.0 μm) had more blisters than the coating with lower thickness (6.0 μm). Lower density of columnar Cr coatings causes less diffusion of Cr atoms into Zr alloy in comparison with dense ones. Other important point is a coating microstructure. The significant role of microstructure on interdiffusion coefficients was shown in [39]. Most likely that the microstructure of Cr coatings obtained by hot target and classical

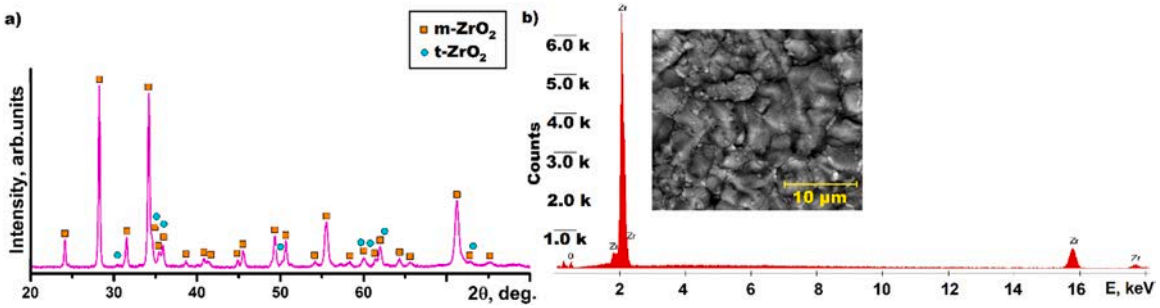

Fig. 11. XRD and EDS spectra of Cr-9d the sample after steam oxidation at 1400 °C for 5 min.

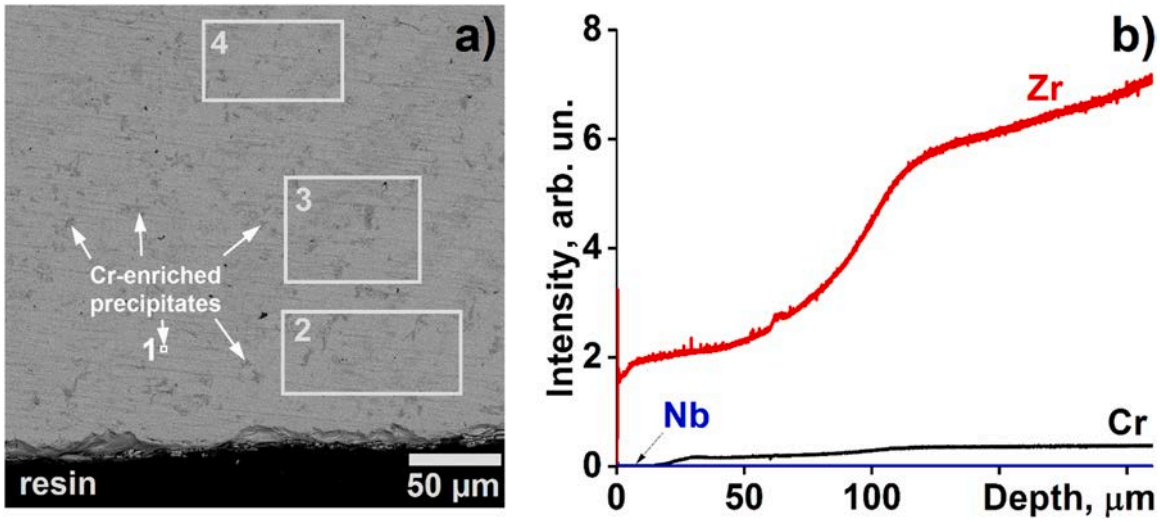

Fig. 12. Cross-section SEM microstructure (a) and GDOES-depth profile (b) of Cr, Zr and Nb in the Cr-coated Zr alloy after annealing in Ar at 1400 °C.

Table 5
The content of Cr and Zr in Cr-coated Zr alloy after annealing in Ar (1400 °C).

	Point 1	Zone 2	Zone 3	Zone 4
Cr, at%	38	6	3	3
Zr, at%	62	94	97	97

sputtering is also influence on interdiffusion kinetics for Cr-Zr system in the present study. As the columnar Cr coatings have a V-shape columns through a coating thickness, it can lead to higher diffusion rate compared to the coatings having coarse-grained columns. Nevertheless, this effect will be investigated in future to detailed discussion.

4. Conclusions

High-temperature oxidation of Cr-coated Zr alloy samples was performed in a steam environment at 900, 1050, 1200 and 1400 °C. The role of microstructure and thickness of the Cr coatings deposited by hot Cr target and multi-cathode magnetron sputtering was discussed. The following conclusions were done.

1. The Cr coatings prepared by hot target magnetron sputtering have a porous microstructure with pronounced columns perpendicular to the surface. The multi-cathode magnetron sputtering provides the formation of Cr coatings with dense microstructure.
2. Cr coatings were consumed by both oxidation of the outer surface in steam and Cr-Zr interdiffusion at the coating-alloy interface. The porous/columnar microstructure of the Cr coatings results in lower activation energy (124 kJ/mol) for Cr oxidation compared to dense coatings (249 kJ/mol). The type of coating microstructure has significant effect on oxidation at temperatures lower 1050 °C.
3. The stabilization of α-Zr phase by oxygen underneath the columnar Cr coating can slow down the Cr-Zr interdiffusion. Less Cr consumption rate by interdiffusion provides the same thickness of the residual Cr layer of the columnar Cr coatings despite the higher chromia scale compared to dense coatings.
4. The fast Cr-Zr interdiffusion kinetics can cause the full Cr coating consumption in the Zr alloy at the Cr-Zr eutectic temperature (1330 °C) and above. This leads to the result that no protective Cr oxide film is formed on the sample surface and direct oxidation of the Zr alloy at 1400 °C. The growth of α-Zr (O) and ZrO_2 layers leads to the diffusion of Cr atoms deeper in the alloy consisting of β-Zr phase.

Funding

The work was supported by the Russian Science Foundation [Grant No. 19-79-10116].

CRediT authorship contribution statement

E.B. Kashkarov: Conceptualization, Investigation, Formal analysis, Visualization, Writing – original draft. **D.V. Sidelev:** Conceptualization, Data curation, Formal analysis, Methodology, Investigation, Writing – review & editing. **N.S. Pushilina:** Investigation, Writing – original draft. **J. Yang:** Investigation, Writing – review & editing. **C. Tang:** Investigation, Writing – review & editing. **M. Steinbrück:** Validation, Formal analysis, Resources, Writing – review & editing.

Declaration of Competing Interest

The authors declare that they have no known competing financial interests or personal relationships that could have appeared to influence the work reported in this paper.

Data Availability

The raw/processed data required to reproduce these findings cannot be shared at this time as the data also forms part of an ongoing study.

Acknowledgements

The authors are grateful to C. Miton for some of the oxidation tests performed. The authors acknowledge the TPU Enhancement Program.

References

[1] A.T. Motta, A. Couet, R.J. Comstock, Corrosion of zirconium alloys used for nuclear fuel cladding, Annu. Rev. Mater. Sci. 45 (2015) 311–343, https://doi.org/10.1146/annurev-matsci-070214-020951.

[2] V. Shishov, The evolution of microstructure and deformation stability in Zr-Nb-(Sn, Fe) alloys under neutron irradiation, in: Zirconium in the Nuclear Industry, in book: Zirconium in the Nuclear Industry: 16th International Symposium, ASTM International, 2012, pp. 37–66.

[3] K.A. Terrani, Accident tolerant fuel cladding development: promise, status, and challenges, J. Nucl. Mater. 501 (2018) 13–30, https://doi.org/10.1016/j.jnucmat.2017.12.043.

[4] C. Tang, M. Stueber, H.J. Seifert, M. Steinbrueck, Protective coatings on zirconium-based alloys as accident-tolerant fuel (ATF) claddings, Corros. Rev. 35 (2017) 141–165, https://doi.org/10.1515/corrrev-2017-0010.

[5] E.J. Opila, N.S. Jacobson, D.L. Myers, E.H. Copland, Predicting oxide stability in high-temperature water vapor, JOM 58 (2006) 22–28, https://doi.org/10.1007/s11837-006-0063-3.

[6] H. Yeom, C. Lockhart, R. Mariani, P. Xu, M. Corradini, K. Sridharan, Evaluation of steam corrosion and water quenching behavior of zirconium-silicide coated LWR fuel claddings, J. Nucl. Mater. 499 (2018) 256–267, https://doi.org/10.1016/j.jnucmat.2017.11.045.

[7] P.J. Doyle, S.S. Raiman, R. Rebak, K.A. Terrani, Characterization of the hydrothermal corrosion behavior of ceramics for accident tolerant fuel cladding, In Proceedings of the 18th International Conference on Environmental Degradation of Materials in Nuclear Power Systems–Water Reactors, Portland, OR, USA, 13–17 August 2017, pp. 269–280. ⟨https://doi.org/10.1007/978-3-030-04639-2_99⟩.

[8] J.-C. Brachet, I. Idarraga-Trujillo, M. Le Flem, M. Le Saux, V. Vandenberghe, S. Urvoy, E. Rouesne, T. Guilbert, C. Toffolon-Masclet, M. Tupin, Early studies on Cr-coated Zircaloy-4 as enhanced accident tolerant nuclear fuel claddings for light water reactors, J. Nucl. Mater. 517 (2019) 268–285, https://doi.org/10.1016/j.jnucmat.2019.02.018.

[9] D.V. Sidelev, E.B. Kashkarov, M.S. Syrtanov, V.P. Krivobokov, Nickel-chromium (Ni–Cr) coatings deposited by magnetron sputtering for accident tolerant nuclear fuel claddings, Surf. Coat. Technol. 369 (2019) 69–78, https://doi.org/10.1016/j.surfcoat.2019.04.057.

[10] E.B. Kashkarov, D.V. Sidelev, M. Rombaeva, M.S. Syrtanov, G.A. Bleykher, Chromium coatings deposited by cooled and hot target magnetron sputtering for accident tolerant nuclear fuel claddings, Surf. Coat. Technol. 389 (2020), 125618, https://doi.org/10.1016/j.surfcoat.2020.125618.

[11] E.B. Kashkarov, D.V. Sidelev, M.S. Syrtanov, C. Tang, M. Steinbrück, Oxidation kinetics of Cr-coated zirconium alloy: effect of coating thickness and microstructure, Corros. Sci. 175 (2020), 108883, https://doi.org/10.1016/j.corsci.2020.108883.

[12] J.-C. Brachet, E. Rouesne, J. Ribis, T. Guilbert, S. Urvoy, G. Nony, C. Toffolon-Masclet, M. Le Saux, N. Chaabane, H. Palancher, A. David, J. Bischoff, J. Augereau, E. Pouillier, High temperature steam oxidation of chromium-coated zirconium-based alloys: kinetics and process, Corros. Sci. 167 (2020), 108537, https://doi.org/10.1016/j.corsci.2020.108537.

[13] H. Liu, Y. Feng, Y. Yao, B. Li, R. Wang, X. Shi, P. Li, J. Shu, F. Huang, Q. Huang, F. Ge, Effect of the 345 °C and 16.5 MPa autoclave corrosion on the oxidation behavior of Cr-coated zirconium claddings in the high-temperature steam, Corros. Sci. 189 (2021), 109608, https://doi.org/10.1016/j.corsci.2021.109608.

[14] X. He, Z. Tian, B. Shi, X. Xu, C. Meng, W. Dang, J. Tan, X. Ma, Effect of gas pressure and bias potential on oxidation resistance of Cr coatings, Ann. Nucl. Energy 132 (2019) 243–248, https://doi.org/10.1016/j.anucene.2019.04.038.

[15] G. Li, Y. Liu, Y. Zhang, H. Li, X. Wang, M. Zheng, Y. Li, High temperature anti-oxidation behavior and mechanical property of radio frequency magnetron sputtered Cr coating, Metals 10 (2020) 1509, https://doi.org/10.3390/met10111509.

[16] C. Azevedo, Selection of fuel cladding material for nuclear fission reactors, Eng. Fail. Anal. 18 (2011) 1943–1962, https://doi.org/10.1016/j.engfailanal.2011.06.010.

[17] Y. Meng, S. Zeng, Z. Teng, X. Han, H. Zhang, Control of the preferential orientation Cr coatings deposited on zircaloy substrates and study of their oxidation behavior, Thin Solid Films 730 (2021), 138699, https://doi.org/10.1016/j.tsf.2021.138699.

[18] J. Jiang, H. Zhai, M. Du, D. Wang, X. Pei, X. Ma, B. Wang, Temperature-dependent deformation and cracking behavior in Cr coating for accident tolerant fuel cladding: an in situ SEM study, Surf. Coat. Technol. 427 (2021), 127815, https://doi.org/10.1016/j.surfcoat.2021.127815.

[19] J. Jiang, M. Yuan, M. Du, X. Ma, On the crack propagation and fracture properties of Cr-coated Zr-4 alloys for accident-tolerant fuel cladding: In situ three-point bending test and cohesive zone modeling, Surf. Coat. Technol. 427 (2021), 127810, https://doi.org/10.1016/j.surfcoat.2021.127810.

[20] J. Liu, C. Tang, M. Steinbrück, J. Yang, U. Stegmaier, M. Große, D. Yun, H. J. Seifert, Transient experiments on oxidation and degradation of Cr-coated Zircaloy in steam up to 1600 °C, Corros. Sci. 192 (2021), 109805, https://doi.org/10.1016/j.corsci.2021.109805.

[21] H.B. Ma, Y.H. Zhao, Y. Liu, J.T. Zhu, J. Yan, T. Liu, Q.S. Ren, Y.H. Liao, G. Liu, X. D. Lin, M.Y. Yao, Self-healing behavior of Cr-coated Zr alloy cladding in high temperature steam oxidation process, J. Nucl. Mater. 558 (2022), 153327, https://doi.org/10.1016/j.jnucmat.2021.153327.

[22] Z. Duan, H. Yang, Y. Satoh, K. Murakami, S. Kano, Z. Zhao, J. Shen, H. Abe, Current status of materials development of nuclear fuel cladding tubes for light water reactors, Nucl. Eng. Des. 316 (2017) 131–150, https://doi.org/10.1016/j.nucengdes.2017.02.031.

[23] M. Steinbrueck, U. Stegmaier, M. Große, L. Czerniak, E. Lahoda, R. Daum, K. Yueh, High-temperature oxidation and quenching of chromium-coated zirconium alloy ATF cladding tubes with and w/o pre-damage, J. Nucl. Mater. 559 (2022) 53470, https://doi.org/10.1016/j.jnucmat.2021.153470.

[24] D.V. Sidelev, G.A. Bleykher, V.P. Krivobokov, Z. Koishybayeva, High-rate magnetron sputtering with hot target, Surf. Coat. Technol. 308 (2016) 168–173, https://doi.org/10.1016/j.surfcoat.2016.06.096.

[25] M. Steinbrück, Oxidation of boron carbide at high temperatures, J. Nucl. Mater. 336 (2005) 185–193, https://doi.org/10.1016/j.jnucmat.2004.09.022.

[26] L. Sepold, P. Hofmann, W. Leiling, A. Miassoedov, D. Piel, L. Schmidt, M. Steinbrück, Reflooding experiments with LWR-type fuel rod simulators in the QUENCH facility, Nucl. Eng. Des. 204 (2001) 205–220, https://doi.org/10.1016/S0029-5493(00)00308-3.

[27] J.A. Thornton, High-Rate thick film growth, Annu. Rev. Mater. Sci. 7 (1977) 239–260, https://doi.org/10.1146/annurev.ms.07.080177.001323.

[28] G. Abadias, E. Chason, J. Keckes, M. Sebastiani, G.B. Thompson, E. Barthel, G. L. Doll, C.E. Murray, C.H. Stoessel, L. Martinu, Review Article: Stress In Thin Films And Coatings: Current status, challenges, and prospects, J. Vac. Sci. Technol. A 36 (2018), 020801, https://doi.org/10.1116/1.5011790.

[29] A.M. Huntz, Stresses in NiO, Cr_2O_3 and Al_2O_3 oxide scales, Mater. Sci. Eng. A 201 (1–2) (1995) 211–228, https://doi.org/10.1016/0921-5093(94)09747-X.

[30] T. Wei, R. Zhang, H. Yang, H. Liu, S. Qiu, Y. Wang, P. Du, K. He, X. Hu, C. Dong, Microstructure, corrosion resistance and oxidation behavior of Cr-coatings on Zircaloy-4 prepared by vacuum arc plasma deposition, Corros. Sci. 158 (2019), 108077, https://doi.org/10.1016/j.corsci.2019.06.029.

[31] J. Yang, U. Stegmaier, C. Tang, M. Steinbrück, M. Große, S. Wang, H.J. Seifert, High temperature Cr-Zr interaction of two types of Cr-coated Zr alloys in inert gas environment, J. Nucl. Mater. 547 (2021), 152806, https://doi.org/10.1016/j.jnucmat.2021.152806.

[32] K. Zeng, M. Hamalainen, R. Luoma, A Thermodynamic assessment of the Cr-Zr system, Int. J. Mater. Res. 84 (1) (1993) 23–28, https://doi.org/10.1515/ijmr-1993-840104.

[33] D.V. Sidelev, S.E. Ruchkin, M.S. Syrtanov, E.B. Kashkarov, I.A. Shelepov, A.G. Malgin, K.K. Polunin, K.V. Stoykov, A.A. Mokrushin, Protective Cr coatings with CrN/Cr multilayers for zirconium fuel claddings, Surf. Coat. Techol., in print.

[34] J.C. Brachet, M. Le Saux, J. Bischoff, H. Palancher, R. Chosson, E. Pouillier, T. Guilbert, S. Urvoy, G. Nony, T. Vandenberghe, A. Lequien, C. Miton, P. Bossis, Evaluation of Equivalent Cladding Reacted parameters of Cr-coated claddings oxidized in steam at 1200 °C in relation with oxygen diffusion/partitioning and post-quench ductility, J. Nucl. Mater. 533 (2020), 152106, https://doi.org/10.1016/j.jnucmat.2020.152106.

[35] L. Bataillou, C. Desgranges, L. Martinelli, D. Monceau, Modelling of the effect of grain boundary diffusion on the oxidation of Ni-Cr alloys at high temperature, Corros. Sci. 136 (2018) 148–160, https://doi.org/10.1016/j.corsci.2018.03.001.

[36] D. Arias, J.P. Abriata, The Cr−Zr (Chromium-Zirconium) system, Bull. Alloy Phase Diagr. 7 (1986) 237–244, https://doi.org/10.1007/BF02868997.

[37] X. Han, J. Xue, S. Peng, H. Zhang, An interesting oxidation phenomenon of Cr coatings on Zry-4 substrates in high temperature steam environment, Corros. Sci. 156 (2019) 117–124, https://doi.org/10.1016/j.corsci.2019.05.017.

[38] X. Han, C. Chen, Y. Tan, W. Feng, S. Peng, H. Zhang, A systematic study of the oxidation behavior of Cr coatings on Zry4 substrates in high temperature steam environment, Corros. Sci. 174 (2020), 108826, https://doi.org/10.1016/j.corsci.2020.108826.

[39] T. Fujita, Z. Horita, T.G. Langdon, Using grain boundary engineering to evaluate the diffusion characteristics in ultrafine-grained Al–Mg and Al–Zn alloys, Mater. Sci. Eng. A 371 (2004) 241–250, https://doi.org/10.1016/j.msea.2003.12.042.